Augmenting immunotherapy via bioinspired MOF-based ROS homeostasis disruptor with nanozyme-cascade reaction

Ruifang Wang[a,b+], *Maosong Qiu*[a,b+], *Lei Zhang*[a,b,c+], *Meiju Sui*[a,b], *Long Xiao*[a,b], *Qiao Yu*[a,b], *Chaohui Ye*[a,b,c], *Shizhen Chen*[a,b,c *], *Xin Zhou*[a,b,c *]

[a] State Key Laboratory of Magnetic Resonance and Atomic and Molecular Physics, National Center for Magnetic Resonance in Wuhan, Wuhan Institute of Physics and Mathematics, Innovation Academy for Precision Measurement Science and Technology, Chinese Academy of Sciences-Wuhan National Laboratory for Optoelectronics, Huazhong University of Science and Technology, Wuhan 430071, P. R. China.

[b] University of Chinese Academy of Sciences, Beijing 100049, P. R. China.

[c] Optics Valley Laboratory, Hubei 430074, P.R. China.

[*] Corresponding author: xinzhou@wipm.ac.cn; chenshizhen@wipm.ac.cn.

[+] These authors contributed equally to this work

ABSTRACT:

Despite its remarkable clinical breakthroughs, immune checkpoint blockade (ICB) therapy remains limited by the insufficient immune response in the “cold” tumor. Nanozyme-based antitumor catalysis is associated with precise immune activation in the tumor microenvironment (TME). In this study, a cascade-augmented nanoimmunomodulator (CMZM) with multienzyme-like activities, which

This article has been accepted for publication and undergone full peer review but has not been through the copyediting, typesetting, pagination and proofreading process, which may lead to differences between this version and the Version of Record. Please cite this article as doi: 10.1002/adma.202306748.

includes superoxide dismutase (SOD), catalase (CAT), peroxidase (POD), and glutathione oxidase (GSHOx), that dissociates under an acidic and abundant GSH TME, is proposed for multimodal imaging-guided chemodynamic therapy (CDT)/photodynamic therapy (PDT) enhanced immunotherapy. Vigorous multienzyme-like activities can not only produce O_2 to alleviate hypoxia and promote the polarization of M2 to M1 macrophages but also generate ROS (•OH and $^1O_2$) and deplete GSH in the TME to expose necrotic cell fragments and reverse immunosuppressive TME by eliciting the maturation of dendritic cells and infiltration of cytotoxic T lymphocytes in tumors. Therefore, inhibitory effects on both primary and distant tumors were achieved through synergy with an α-PD-L1 blocking antibody. This cascade multienzyme-based nanoplatform provides a smart strategy for highly efficient ICB immunotherapy against "cold" tumors by revising immunosuppressive TME.

1. Introduction

Cancer immunotherapy has emerged as one of the most promising therapies and numerous advanced malignancies have been treated successfully with immunotherapy.[1] Cancer treatment has undergone a revolutionary shift because of immune checkpoint blockade (ICB) which targets immunosuppressive proteins, including programmed cell death ligand 1 (PD-L1).[2] However, because of the complexity, diversity, and heterogeneity of the tumor microenvironment (TME) and inactivation of the host immune system, ICB strategies cannot induce systemic antitumor responses in immunosuppressive tumors such as triple-negative breast cancer.[3] The challenge in immunotherapy is reversing the immunosuppressive TME of tumors and enhancing the immune response.[4]

Immunosuppressive TME is characterized by moderate acidity, overexpressed glutathione (GSH), hypoxia, low immunogenicity T cell infiltration, along with poor antigen presentation efficiency,[5] and therefore, the appropriate strategy to reprogram immunologically "cold" tumors towards "hot" tumors can be designed to reinvigorate the immune response. For example, photodynamic therapy (PDT)/chemodynamic therapy (CDT) can generate cytotoxic reactive oxygen species (ROS), which lead to the apoptosis and necrosis of tumors cells, elevating antitumor efficiency by promoting the exposure of tumor-associated antigens (TAAs) for immunogenic T cell infiltration.[6] However, ROS production by CDT/PDT is limited by TME, highlighting an insufficient level of H_2O_2 (1 mM) or O_2. Combined with overexpressed cellular GSH (~10 mM), insufficient apoptotic cell fragments have an inferior effect on immune activation at the expense of CDT/PDT efficiency.[7] Although substantial TME-responsive nanohybrids have been constructed for enhancing antigen-specific immunological responses by boosting abundant H_2O_2/O_2 and GSH elimination, few reports on nanomaterials can advance ROS yield and utilization in an all-around manner.

Recently, nanozymes have gained considerable attention for their outstanding stability and convertible catalytic activities, similar to those of natural enzymes such as superoxide dismutase (SOD), catalase (CAT), glutathione peroxidase (GPx), peroxidase (POD), and glutathione oxidase (GSHOx).[8] Superoxide anions ($O_2^{\bullet-}$) are converted into H_2O_2 by SOD. Consequently, the generated H_2O_2 is converted to O_2 and •OH through reactions catalyzed by CAT and POD, respectively. Finally, H_2O_2 is transferred into H_2O by GPx using GSH.[9] Based on these characteristics, an H_2O_2 homeostasis disruptor can be designed to increase the concentration of H_2O_2 in the immunosuppressive TME by increasing its yield and inhibiting its degradation. With GSH elimination by GSHOx, •OH generated by CDT via a Fenton/Fenton-like reaction (Fe^{2+}/Mn^{2+} + H_2O_2 → Fe^{3+}/Mn^{3+} + •OH + OH^-) and $^1O_2$ produced by PDT under laser irradiation can destroy tumor cells more effectively.[10] Finally,

sufficient tumor cell fragments, such as TAAs, are presented to cytotoxic T lymphocytes (CTLs) by dendritic cells (DC), which leads to the activation and infiltration of CTLs in the TME. However, an excellent nanozyme that disrupts ROS homeostasis in all directions is yet to be combined with ICB to improve immunotherapy efficacy.

In this study, an innovative ROS homeostasis disruptor (CMZM) is proposed in combination with ICB for synergistic CDT, PDT, and immunotherapy (Scheme 1). In this system, a multifunctional nanozyme based on CMZM can be applied to generate H_2O_2, O_2, and •OH and consume GSH, thereby revising immunosuppression in the TME. CMZM can collapse under overexpressed GSH and acidic conditions in the TME, accelerating the release of Mn ions and chlorin e6 (Ce6), which is beneficial for the generation of $^1O_2$. Simultaneously, this leads to a remarkably enhanced $^{19}F/^1H$ T_1-weighted dual-nuclei magnetic resonance imaging (MRI) contrast. Consequently, the H_2O_2 balance is ultimately disturbed, which results in abundant ROS in cancer cells to boost CDT and PDT productivity. In addition, the new TAAs released by CDT and PDT can activate CTLs and promote their infiltration into tumors, which, with the aid of PD-L1 checkpoint blockade, can inhibit tumor growth at distant sites. These results highlight the potential of disrupting ROS homeostasis in all directions using smart nanozyme to improve the therapeutic efficacy of ICB immunotherapy.

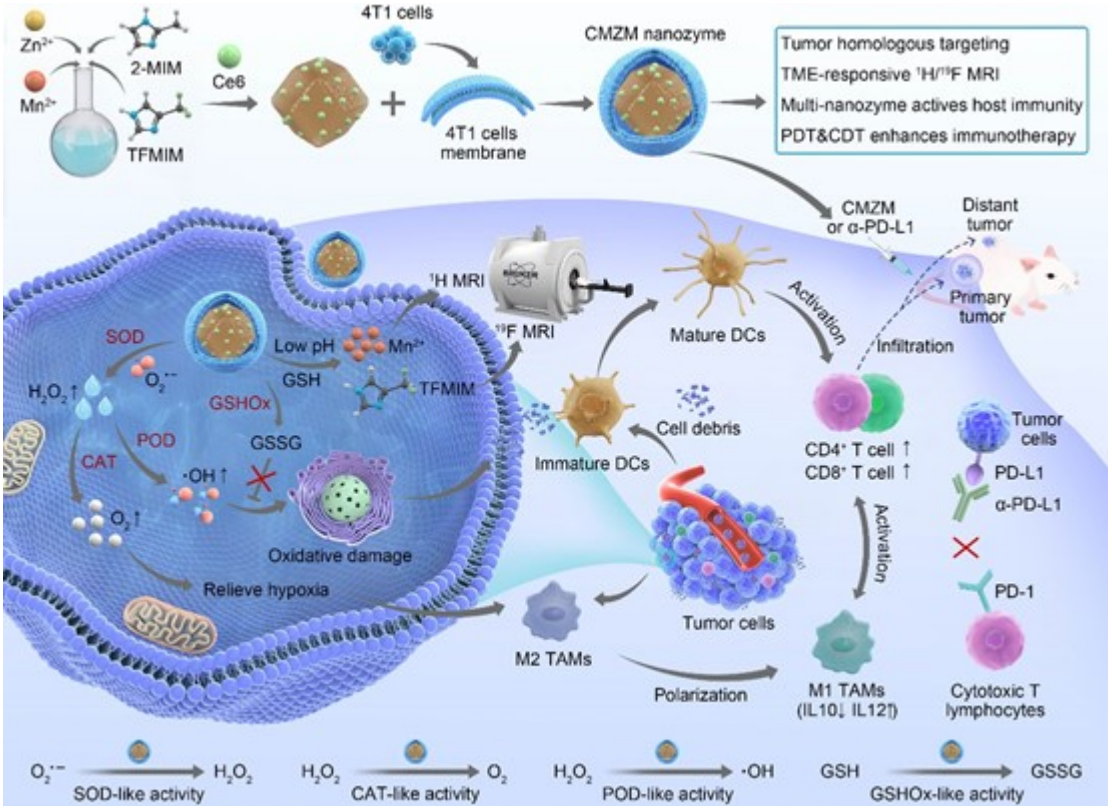

Scheme 1. Schematic illustration of the fabrication of CMZM and TME-activated enzymatic cascade catalytic-boosted immunotherapy combined with α-PD-L1. After homologous targeting to tumor tissue, the immunosuppressive TME could be reversed by the multienzyme-mimic activities of CMZM to augment immunotherapy by synergism with PD-L1 checkpoint blockade.

2. Results and Discussion

2.1 Fabrication and Characterization of CMZM

Scheme 1 illustrates the synthesis procedure for CMZM, and the details are outlined in the Supporting Information. Similar to the fabrication of the zeolitic imidazolate framework-8 (ZIF-8),[11] a CMZ without a 4T1 cell membrane (Mem) coating was constructed by replacing part of the ligand 2-

methylimidazole (2-MIM) with 4-(trifluoromethyl)-1H-imidazole (TFMIM) and doping with Mn ions. After stirring with Ce6, the Ce6 was loaded into the MZ (CMZ). Transmission electron microscopy (TEM) results indicated that the morphology of CMZ was similar to that of ZIF-8, with an average particle size of 180 nm (Figure 1a,b). After coating the CMZ surface with Mem, the average diameter of CMZM increased to 264 nm. Both the analogous protein band between CMZM and Mem and the membrane proteins CD44 and CD47 observed in CMZM confirmed successful decoration with Mem (Figure 1c and Figure S1). Elemental mapping results confirmed that the nanozyme consisted of Mn, F, Zn, and N (Figure 1d). Unlike ZIF-8 and CMZ, the positive charge of CMZM was neutralized by decoration with Mem. The surface charge of CMZM was reversed under mildly acidic conditions regardless of the presence or absence of GSH, which suggests that CMZM is prone to internalization by tumor cells in the TME (Figure 1e). X-ray diffraction (XRD) results demonstrated that Mn ions were uniformly doped on the ZIF-8 crystal lattice, and this was authenticated by the absence of obvious diffraction peaks of other impurity phases observed in CMZ (Figure 1f).[12] Previous studies showed that the nanozyme activity of Mn-based nanomaterials is rooted in the various valence states of the Mn ions.[13] The presence of Mn^{2+} (640.1 eV), Mn^{3+} (641.1 eV), and Mn^{4+} (642.2 eV) was confirmed by the XPS analysis of CMZM, providing encouraging evidence of CMZM nanozyme performance (Figure 1g,h). Subsequently, a photosensitizer Ce6 was loaded into the MZ based on its pore size (Figure S2) to endow it with PDT capability; the loading ratio was calculated to be 76.4% using a UV–vis–NIR spectrometer (Figure 1i). The TME-responsive collapse behavior of CMZ was demonstrated using TEM images of CMZ cultured in acidic solutions with or without GSH (10 mM). Compared to ZIF-8 nanoparticles, CMZ with the introduction of Mn is more difficult to be collapsed (Figure S3). CMZM was investigated in a solution at various pH values and in the presence of GSH (10 mM) to evaluate the Ce6 release behavior in the TME. In contrast to the sluggish Ce6-release behavior of CMZM at pH

7.4, the release rates of Ce6 were found to be faster in acidic solutions at pH 6.5, 5.5, and pH 5.5 plus GSH (10 mM) (Figure 1j). These results confirm that CMZM is a promising acidic/GSH-responsive nanozyme with multienzyme-like activities.

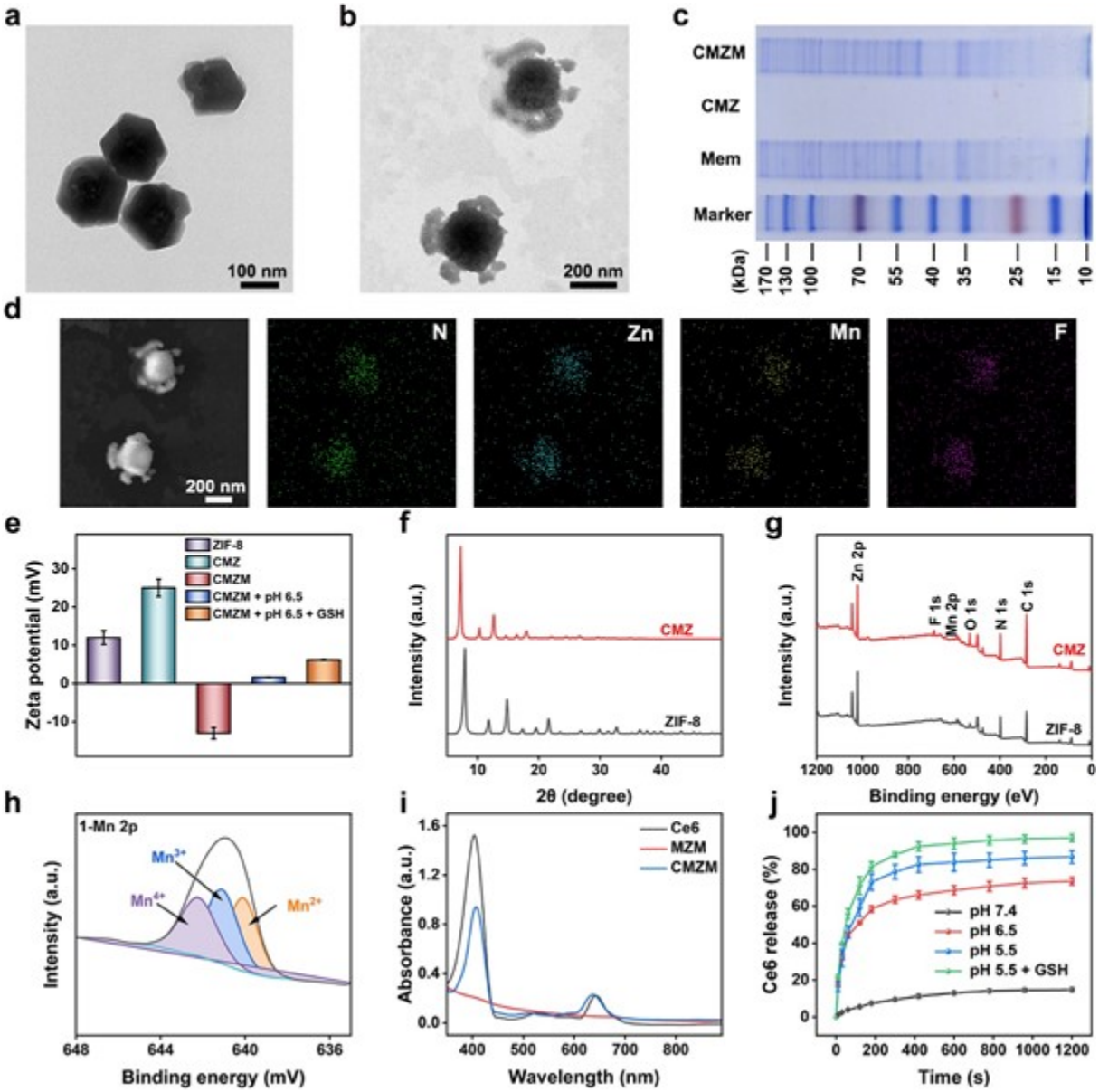

Figure 1. Characterization of CMZM. (a,b) TEM images of (a) MZ and (b) CMZM. (c) SDS-PAGE protein analysis of Mem, CMZ, and CMZM. (d) STEM and corresponding elemental mapping of CMZM (scar bar:

50 μm). (e) Zeta potential of ZIF-8, CMZ, CMZM, CMZM (pH 6.5), and CMZM (pH 6.5 + 10 mM GSH). (f) XRD of ZIF-8 and CMZ. (g) XPS spectra of ZIF-8 and MZ. (h) Mn2p XPS analysis of MZ. (i) UV–vis–NIR absorption spectra of Ce6, MZM, and CMZM. (j) Cumulative release of Ce6 from CMZM incubated at different conditions (mean ± SD, *n* = 3).

The multienzyme-like activity and MRI performance of CMZM were evaluated (Figure 2a). To this end, the SOD-like activity of CMZM was assessed using Cu/Zn-SOD and Mn-SOD assay kits with WST-8. In brief, WST-8 reacts with $O_2^{\bullet-}$ produced by xanthine oxidase to produce formazan with a robust UV–vis absorbance at 450 nm. Once CMZM was added, the intensity of the UV–vis absorbance declined rapidly with increasing CMZM concentration, confirming the concentration-dependent SOD-like activity of CMZM (Figure 2b). Subsequently, the self-supplied H_2O_2 in the tumor was degraded to O_2 and H_2O via CAT-like activity, which was helpful in reversing the tumor immunosuppressive microenvironment by relieving tumor hypoxia. Thus, the CAT-like activity of CMZM was determined using a dissolved oxygen meter. O_2 gas was observed on mixing CMZM (50 μg mL^{-1}) with H_2O_2 (50 mM), and its density increased over time (Figure 2c). These results illustrate that CMZM can alleviate tumor hypoxia via CAT-like activity.

Loading CMZM with the photosensitizer Ce6 afforded CMZM a PDT effect. Next, the generation of $^1O_2$ was monitored by UV–vis–NIR absorbance attenuation of 1,3-Diphenylisobenzofuran (DPBF) on 660 nm laser irradiation (0.1 W cm^{-2}). A significant decrease in UV–vis–NIR intensity was observed in the CMZM plus H_2O_2 (10 mM) group upon laser irradiation because of the abundant O_2 produced by the CAT-like activity of CMZM (Figures 2d and S4). Electron spin resonance (ESR) displayed a featured spectrum of 1:1:1, which was attributed to the generation of $^1O_2$ (Figure S5).

Moreover, the abundant H_2O_2 in the tumor can be catalyzed to •OH by a POD-like nanozyme used for the CDT of tumors. Consequently, the POD-like activity was monitored using methylene blue (MB), which can be degraded by •OH. As expected, CMZM and H_2O_2 showed no difference in the UV–vis–NIR absorbance of MB; however, the intensity of the UV–vis–NIR absorbance of MB declined sharply after mixing CMZM with H_2O_2 (10 mM) in a $NaHCO_3$ solution (25 mM) for 30 min, demonstrating that •OH was produced by the CMZM-mediated Fenton-like reaction. Further, the generated •OH (a featured spectrum of 1:2:2:1) was confirmed by ESR (Figure S6). The UV–vis–NIR absorbance of MB exhibited negligible decrement after equal operation in the PB buffer (pH = 7.4), which showed the critical value of HCO_3^- in the CMZM-mediated Fenton-like reaction and the biosafety of the *in vivo* application (Figure S6). The POD-like activity of different concentrations of CMZM is determined using the UV-Vis-NIR method, as shown in Figure 2e. The depletion of MB was linearly related to the CMZM concentration (Figure 2g). In addition to the UV–vis–NIR method, the introduction of TFMIM into CMZM enabled the detection of (POD) activity using ^{19}F NMR. These findings revealed a progressive enhancement of the ^{19}F NMR signal at −61.7 ppm, resulting from the release of TFMIM in CMZM with an increase in the concentration of CMZM (Figure 2f). This trend agrees well with the results obtained from UV–vis–NIR spectroscopy, which validates the applicability of ^{19}F NMR for assessing the POD-like activity (Figure 2g).

Although abundant ROS were generated by CMZM, the overexpression of GSH (~10 mM) in the tumor could help prevent damage. The GSH-eliminating capability of CMZM by the GSHOx-like activity was assessed using 5,5′-dithiobis-(2-nitrobenzoic acid) (DTNB) because of the existence of high valence Mn ion; DTNB is a GSH indicator that reacts with GSH to yield a colored product. After adding CMZM to a mixed solution of GSH and DTNB, the intensity of the UV–vis absorbance at 412 nm decreased with an increase in the amount of CMZM (Figure 2h), confirming the robust GSHOx-

like activity of CMZM. The elimination of GSH is positively correlated with CMZM concentration (Figure 2j). In addition, ^{19}F NMR was used to determine the GSHOx-like activity of CMZM, and as expected, a CMZM concentration-dependent ^{19}F NMR signal enhancement was observed (Figure 2i). The tendency of ^{19}F NMR signals is in good agreement with the UV–vis spectroscopic results, which guarantees the application of ^{19}F NMR for detecting GSHOx-like activity (Figure 2j). TEM results showed that the collapse of CMZ was insensitivity to SOD-like and CAT-like activities (Figure S7), which lead to the failure to monitor SOD-like and CAT-like activities by ^{19}F NMR. Even though the traditional technique for enzymatic activity detection is using optical methods with the advantage of simplicity and convenience, it is not capable of *in vivo* application. In contrast, the ^{19}F MR technique, with unlimited tissue depth penetration and without endogenous interference, has considerable potential for the *in vivo* monitoring of enzymatic activities, which provides an alternative approach to optical methods.

The ROS generated by CMZM can induce serious oxidative damage with the consumption of GSH, which helps enhance the local immune response of the tumor. These results confirm that CMZM was equipped with excellent multienzyme activities of SOD-like, CAT-like, POD-like, and GSHOx-like nanozymes, which could not only self-supply adequate H_2O_2 and O_2 but also generate sufficient ROS and consume GSH, thereby leading to the potential of breaking the tumor reductive and immunosuppressive microenvironment defense.

Considering that Mn-based nanomaterials have been extensively used as T_1-weighted MRI contrast agents (CAs) for diagnosing tumors,[15] Mn ions released from CMZM were explored at various pH values or in the presence of GSH (10 mM). Similar to the release profiles of Ce6 (Figure 1j), the fastest release of Mn ions was observed at pH 5.5 and the GSH condition was also observed (Figure S8). Correspondingly, a negligible T_1-weighted MRI signal was observed in CMZM at pH 7.4, and the

initial longitudinal relaxivity (r_1) was 0.50 mM^{-1} s^{-1}. In contrast, the r_1 of CMZM at pH 6.5, pH 5.5, and pH 5.5 plus GSH (10 mM) increased to 2.56, 4.58, and 5.46 mM^{-1} s^{-1}, respectively (Figures 2k and S9). The ^{19}F magnetic resonance performance of the CMZM was investigated under the same conditions as the ^{1}H T_1-weighted MRI to overcome the drawback of the ^{1}H MRI background signal in the tissue.[16] The intensities of ^{19}F NMR at pH 7.4, 6.5, 5.5, and pH 5.5 plus GSH (10 mM) gradually increased (Figure S10). Correspondingly, the transverse relaxation time (T_2) of TFMIM in CMZM increased upon exposure to a low pH and high GSH concentration (10 mM) condition (Figure S11). The ^{19}F MRI of CMZM under acidic plus GSH conditions displayed the highest contrast effect (Figure 2l), and it is well-known that the ZIF-8-based and Mn-based nanomaterials can decompose under acidic and GSH conditions, respectively.[17] CMZM was prepared by the coordination of Zn^{2+}/Mn^{2+} and 2-MIM/TFMIM, which made the acidic/GSH dual-responsive behavior of CMZM reasonable. According to the TEM images of CMZM under different conditions (Figure S3) and the literature report,[18] the highest ^{19}F MRI contrast under pH 5.5 plus GSH conditions was confirmed. These experimental results suggest that CMZM is a promising TME-responsive multifunctional nanozyme for the early diagnosis of tumors using ^{1}H/^{19}F dual-nuclei MRI.

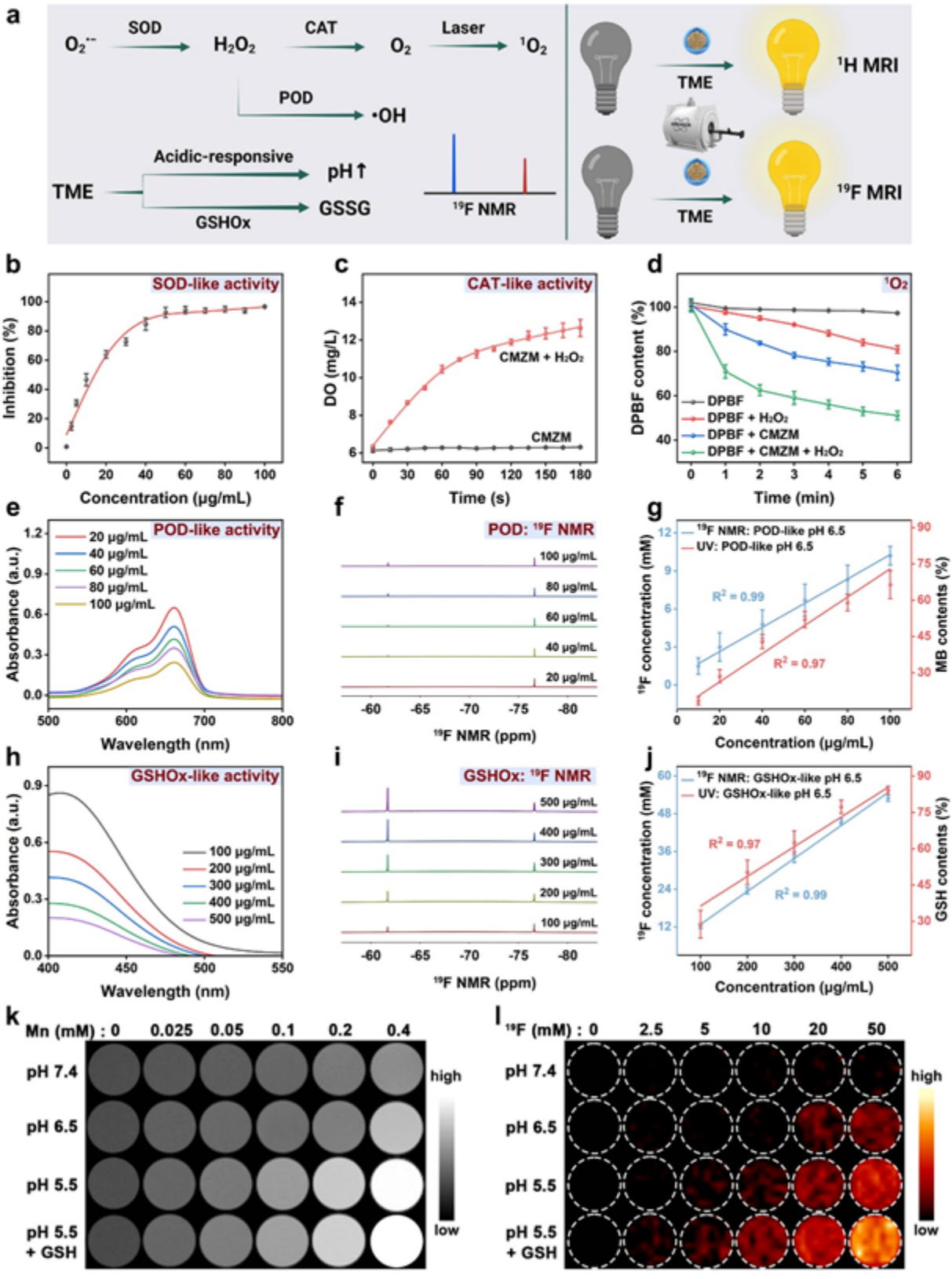

Figure 2. The multienzyme-like activities and MRI performance of CMZM. (a) Diagram for the multienzyme-like activities and TME-responsive $^{19}F/^{1}H$ T_1-weighted MRI of CMZM. (b) The SOD-like activity (mean ± SD, *n* = 3) and (c) the CAT-like activity of CMZM (mean ± SD, *n* = 3). (d) Time-dependent DPBF degradation curves for CMZM with or without H_2O_2 (0.1 mM) under 650 nm laser irradiation (0.1 W cm^{-2}) (mean ± SD, *n* = 3). (e) MB probe caused by CMZM under acidic conditions for •OH generation detection (pH = 6.5). (f) The ^{19}F NMR of different concentrations of CMZM plus H_2O_2 at pH 6.5 (CF_3CH_2OH: -76.6 ppm). (g) Concentration-dependent MB depletion and ^{19}F NMR signals enhancement by CMZM in (e) and (f) (mean ± SD, n = 3). (h) DTNB probe caused by CMZM under acidic conditions for GSH depletion detection (pH = 6.5). (i) The ^{19}F NMR of different concentrations of CMZM at pH 6.5 plus 10 mM GSH (CF_3CH_2OH: -76.6 ppm). (j) Concentration-dependent GSH depletion and ^{19}F NMR signals enhancement by CMZM in (h) and (i) (mean ± SD, *n* = 3). (k) ^{1}H T_1-weighted MRI, and (l) ^{19}F MRI images of various concentrations of CMZM at different pH values with or without GSH (10 mM).

2.2 Cellular Endocytosis, ROS Generation, and CDT&PDT of CMZM

The therapeutic efficacy of CMZM was studied at the cellular level because of its distinguished ROS-generating and GSH-eliminating abilities. The intracellular endocytosis of CMZM at different times was evaluated before performing detailed cell assays. The amount of internalized CMZM increased with an increase in incubation time. According to the quantitative analysis of CLSM images and flow cytometry (FCM), the maximum fluorescence intensity in 4T1 cells was observed after incubation for 4 h (Figure S12). 4T1 cell-based multicellular spheroids (MCSs) were constructed to evaluate the tumor penetration performance of CMZM. Interestingly, CMZM was distributed around the outer border of the MCSs after incubation for 2 h at pH 7.4, suggesting the limited penetration of CMZM because of its relatively large size and negative charge. The red fluorescence emitted via CMZM was

dispersed extensively over MCSs at pH 6.5 2 h post-incubation, indicating excellent tumor infiltration. Further, the infiltration trend was enhanced at pH 6.5 plus 10 mM GSH 2 h post-incubation, as demonstrated by the strong red fluorescence widely dispersed over the whole MCSs, which confirms the TME-enhanced tumor infiltration of CMZM (Figure 3a). These outcomes collectively revealed that CMZM has an outstanding tumor penetration capability beneficial for overcoming biobarriers and improving drug delivery efficiency.

Previous investigations showed that the decoration of tumor cell membranes can endow nanomaterials with homologous targeting capabilities to solid tumors.[19] Intracellular endocytosis in different cells was explored using CMZ with or without 4T1 cell membrane modification for verifying the homotypic targeting capacity of CMZM. Interestingly, the cellular internalization efficiency of CMZM was considerably higher than that of CMZ in 4T1 cells (Figure S13), which was confirmed by the CLSM and FCM analysis. The fluorescence intensity of 4T1 cells was stronger than that of two representative nonhomologous cancer cells (HeLa and A549 cells) after incubation with CMZM (Figure S14), which suggests that the inherent homotypic targeting capability of CMZM with Mem modification. Besides the role of homologous targeting, CLSM and FCM results showed that CMZM decorated with Mem could reduce phagocytosis by macrophages (Figure S15), which contributes to prolonging the blood circulation time for *in vivo* applications. The biocompatibility of CMZM is vital to guarantee its therapeutic effect for biomedical applications. The viability of normal and nonhomologous tumor cells, as determined by the CCK8 assay, displayed insignificant cytotoxicity, which illustrated the notable biocompatibility of CMZM. In comparison, the viability of 4T1 cells showed a declining trend with an increase in the amount of CMZM, and this was attributed to the homologous targeting performance after 4T1 cell membrane modification (Figure S16). To assess the MRI capacity of the CMZM at the cellular level, ^{1}H T_1-weighted/^{19}F MRI was performed on 4T1 cells.

After incubation with CMZM for various periods, 4T1 cells were lysed with lysate to perform ^{1}H T_1-weighted/^{19}F MRI. The results demonstrated that both signal intensities of ^{1}H/^{19}F MRI were positively correlated with incubation time (Figure S17).

The generation of intracellular ROS, including •OH and $^{1}O_2$, was evaluated by 2′,7′-dichlorofluorescein diacetate (DCFH-DA) after various treatments to evaluate the CMZM-mediated CDT and PDT effect *in vitro*. In the presence of ROS, DCFH-DA is oxidized to produce bright green fluorescence. Based on the fluorescence intensity of the CLSM images, the total ROS production was improved significantly in the presence of CMZM with or without laser irradiation (0.1 W cm^{-2}, 5 min) (Figure 3b,c). Subsequently, the *in vitro* CDT and PDT effects of 4T1 cells were analyzed by live/dead cell staining with calcein-AM/PI and a related CCK8 assay. The Ce6 group with laser irradiation (0.1 W cm^{-2}, 5 min) showed a weak cytotoxicity of 17.6% through insufficient ROS production; however, the cytotoxicity substantially improved to 55.7% and 73% in the CMZM and CMZM plus laser groups, respectively, which was attributed to the superior ROS generation capacity of CMZM. Correspondingly, obvious red fluorescence was observed in the CMZM and CMZM plus laser groups (Figure 3d,e). The *in vitro* therapeutic efficacy was further quantified by FCM with Annexin V-FITC/PI staining in 4T1 cells. Following an analogous outcome, cell death was inconspicuous in the PBS, Ce6, and Ce6 + laser groups. The 4T1 cells in the CMZM and CMZM plus laser groups showed palpable cell death (50.95% and 65.57%, respectively) (Figure S18). These results confirm that CMZM can be taken up by 4T1 cells via homologous targeting performance and generate abundant ROS in tumor cells by multienzyme-like activities, which is expected to enhance the CDT and PDT effects of tumors *in vivo* and activate local immune responses of tumors by promoting the exposure to TAAs.

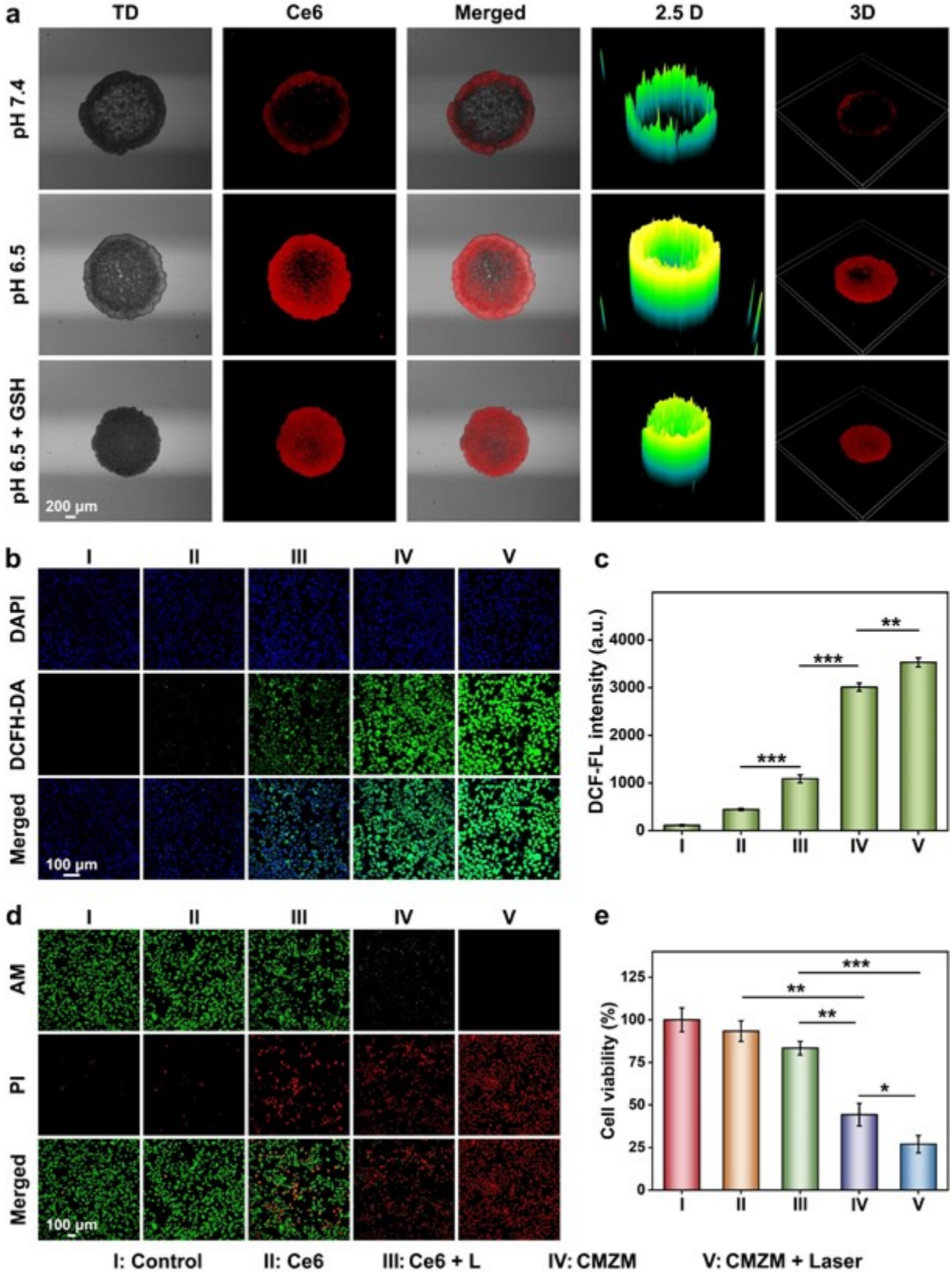

Figure 3. Tumor penetration studies, ROS generation, and CDT&PDT-mediated tumor cell apoptosis of CMZM. (a) Tumor penetration images of CMZM in the 4T1 cell-based multicellular spheroids after respective incubation at pH 7.4, pH 6.5, or pH 6.5 plus GSH (10 mM) for 2 h. (b) CLSM images of ROS generation in 4T1 cells after different treatments and (c) the corresponding fluorescence intensity analysis (mean ± SD, n = 3, **p < 0.01, ***p < 0.001). (d) CLSM images of 4T1 cells staining with Calcein-AM/PI, and (e) the cell viability of 4T1 cells after various treatments (mean ± SD, n = 3, *p < 0.05, **p < 0.01, ***p < 0.001).

2.3 *In Vivo* FLI/^{1}H T_1-Weighted/^{19}F MRI Performance of CMZM

A hemolysis assay was performed to confirm the feasibility of CMZM use *in vivo*. The hemolysis rate of CMZM was less than 5% at a concentration of 1.0 mg mL^{-1} (Figure S19), which guarantees the safe use of nanohybrids *in vivo*. Next, the *in vivo* distribution of CMZM in 4T1 tumor-bearing BALB/c mice was monitored using fluorescence and MR dual-mode imaging. Fluorescence imaging (FLI) demonstrated that CMZM accumulation increased in the tumor region, reached a peak level at 8 h post-injection, and then, it gradually diminished with time. In contrast, the CMZ and free Ce6 groups showed fewer tumors throughout the experimental period (Figure 4a,b and Figure S20a), suggesting better tumor targeting by CMZM. According to the semi-quantitative *ex vivo* imaging of the heart, liver, spleen, lung, kidney, and tumor collected 36 h post-injection, the average fluorescence intensity of the tumor in the CMZM group was 3.9- and 13.3-fold higher than that in the MFZ and free Ce6 groups, respectively. The liver and spleen uptake of CMZM was lower than that of CMZ, which illustrates that CMZM decorated with 4T1 cell membranes could achieve immune escape and upregulate tumor-targeting effects (Figure S20b,c).

Based on the superior *in vitro* MRI performance, T_1-weighted MRI was performed on 4T1 tumor-bearing mice after the *i.v.* injection of CMZM. Interestingly, enhanced contrast in the tumor region was observed on T_1-weighted MRI. According to the quantitative analysis, the T_1-weighted MR signal in the tumor region was enhanced two-fold in the tumor at 8 h post-injection (Figure 4c,d), thereby indicating a high uptake of CMZM in the tumor, which was consistent with the *in vivo* FLI results. Furthermore, obvious T_1-weighted signals were observed in the kidneys (Figure 4e and Figure S21), and they illustrated the effective renal clearance of Mn ions dissociated from CMZM. Thus, both FLI- and T_1-weighted MRI confirmed that Mem-decorated CMZM loaded with Ce6 showed efficient active targeting of tumor cells. Although the primary metabolic pathways differ between free Ce6 (liver metabolism) and Mn ions (kidney metabolism), the highest-intensity time points of FLI and MRI occurred simultaneously. Unlike free Ce6 or Mn ions, the homologous targeting performance of CMZM endowed it with a personalized *in vivo* fate. After internalization by tumor cells, CMZM collapsed, and Mn ions and loaded Ce6 were released gradually. Metabolites in the TME are difficult to eliminate because of the relative immaturity and instability of the aberrant tumor vasculature.[20] Based on experimental outcomes and theoretical analysis, we conjecture that Mn ions and Ce6 released from CMZM could reside in the tumor tissues for a period, which finally leads to the uniform highest intensity time point of FLI and MRI, which is consistent with previous reports.[21] To further evaluate TME-activated ^{19}F MRI, CMZM was injected intratumorally. As expected, the ^{19}F signal was probed as a “hot spot” image with zero background signal in the tumor area (Figure 4f). The results demonstrate that CMZM possesses superior tumor imaging capabilities.

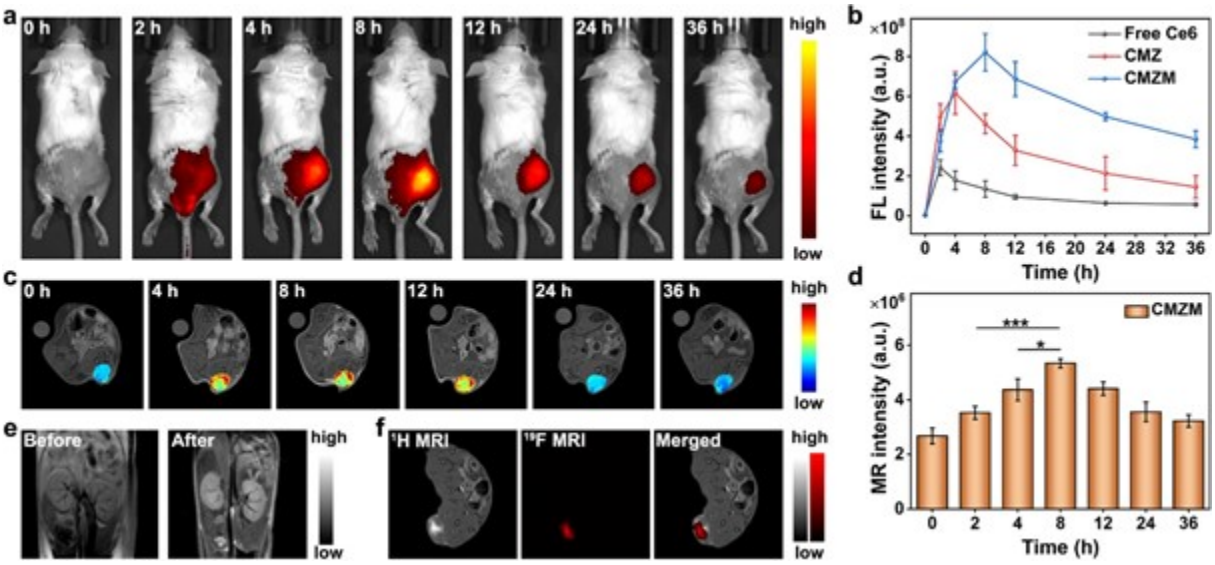

Figure 4. *In vivo* FLI/^{1}H T_1-weighted/^{19}F MRI of CMZM. (a) Time-dependent fluorescence imaging of subcutaneous 4T1 tumor-bearing mice after *i.v.* injection of CMZM. (b) The fluorescence intensity of CMZM, CMZ, and free Ce6 in the tumor area as a function of time (mean ± SD, n = 3). (c) ^{1}H T_1-weighted MRI of subcutaneous 4T1 tumor after *i.v.* injection of CMZM and (d) the corresponding ^{1}H MRI signal intensity of the tumor region as a function of time (mean ± SD, n = 3, ***p < 0.001). (e) ^{1}H T_1-weighted MRI of mice before and 8 h post *i.v.* injection of CMZM displayed in the longitudinal section. (f) ^{1}H T_1-weighted/^{19}F dual-nuclei MRI of subcutaneous 4T1 tumor after intratumoral injection of CMZM.

2.4 *In Vitro* and *In Vivo* Immune Activation of CMZM

A key point that leads to immunosuppressive TME is adequate M2 macrophages being infiltrated in the "cold" tumor.[22] A promising technique for reversing immunosuppression in cancer immunotherapy is inducting macrophages from the M2 to M1 phenotype.[23] Previous studies suggested that increased ROS production may induce oxidative stress.[24] Therefore, inspired by the outstanding ability of CMZM to generate ROS, immune activation experiments were performed using

4T1 cells. RAW264.7 macrophages were treated with interleukin 4 (IL-4) to establish M2 macrophages to confirm the polarization of tumor-associated macrophages (TAMs) induced by CMZM. The RAW264.7 macrophages were co-cultured with 4T1 cells receiving different treatments in the transwell insert system, and the proportion of M2 and M1 macrophages was analyzed by FCM (Figure S22). Compared with the control, the proportion of M2 macrophages in the CMZM and CMZM + laser groups decreased significantly from 45.47% to 36.60% and 30.20%, respectively; the proportion of M1 macrophages increased from 52.80% to 58.80% and 65.50%, respectively (Figure S23a,b). The levels of interleukin 10 (IL-10) secreted by M2 macrophages and interleukin 12 (IL-12) secreted by M1 macrophages, respectively, were determined using ELISA kits. Similarly, the levels of IL-10 and IL-12 in the CMZM and CMZM plus laser groups exhibited a trend consistent with that of M2 and M1 macrophages (Figure S23c); these results demonstrated that CMZM could effectively stimulate M2 macrophages to differentiate into M1 macrophages for reversing the immunosuppressive TME.

Given its excellent ability to ameliorate immunosuppressive TME at the cellular level, the immune activation of CMZM was further evaluated using 4T1 tumor-bearing mice. After treatment with PBS, CMZM, or CMZM plus laser, tumors in various groups were extracted and digested into a single-cell suspension; subsequently, immune-related cells were stained with various antibodies and analyzed using FCM (Figure S24). In contrast with the PBS group, M2 macrophages experienced a noticeable decrease in the CMZM and CMZM plus laser groups (9.94% to 4.71% and 3.42%). The number of polarized M1 macrophages increased significantly from 7.45% to 11.90% and 16.97% in the CMZM and CMZM + laser groups, respectively (Figure 5a,f). The polarization efficiency of M1 macrophages suggested that CMZM and CMZM plus laser effectively transformed the immunosuppressive TME into an immune-supportive state. A previous investigation revealed that nanohybrids with smart

designs could activate the host immune system by augmenting the maturation and migration of dendritic cells. [25] As professional antigen-presenting cells, dendritic cells with abundant antigen information can induce antitumor immunity, which can lead to the significant stimulation of T cell proliferation.[26] Thus, we hypothesized that these excellent nanozymes could activate tumor-specific immune responses. The ability of CMZM to activate immune responses was further validated by monitoring DC maturation and T-cell infiltration. Compared to the control group, the proportion of DC maturation in the tumor was prominently elevated in the CMZM and CMZM + laser groups. The percentage of mature DC increased from 33.10% to 51.60% and 75.60%, respectively (Figure 5b,g). In addition, many Tregs ($CD25^+FOXP3^+$) (50.70%) and a small proportion of $CD4^+$ and $CD8^+$ T cells (23.00% and 7.77%, respectively) were observed in the control group, and they were ascribed to the innate immunosuppressive TME. The percentage of Treg cells decreased to 38.20% and 27.20%, and the percentages of $CD3^+CD4^+$ (30.50% and 44.20%) and $CD3^+CD8^+$ (12.80% and 25.90%) tumor-infiltrating T cells displayed a distinct increase in the CMZM and CMZM + laser groups (Figure 5c–e,h–j), thereby revealing a severe local immune response in the tumor. These results illustrate that CMZM, with or without laser irradiation, can ameliorate immunosuppressive TME to profitable antitumor immunity, and this can lead to the polarization of M2 macrophages to M1 macrophages. TAAs released from necrotic 4T1 tumor cells can be engulfed by DC, which promotes DC maturation and infiltration of CTLs in tumor tissues.

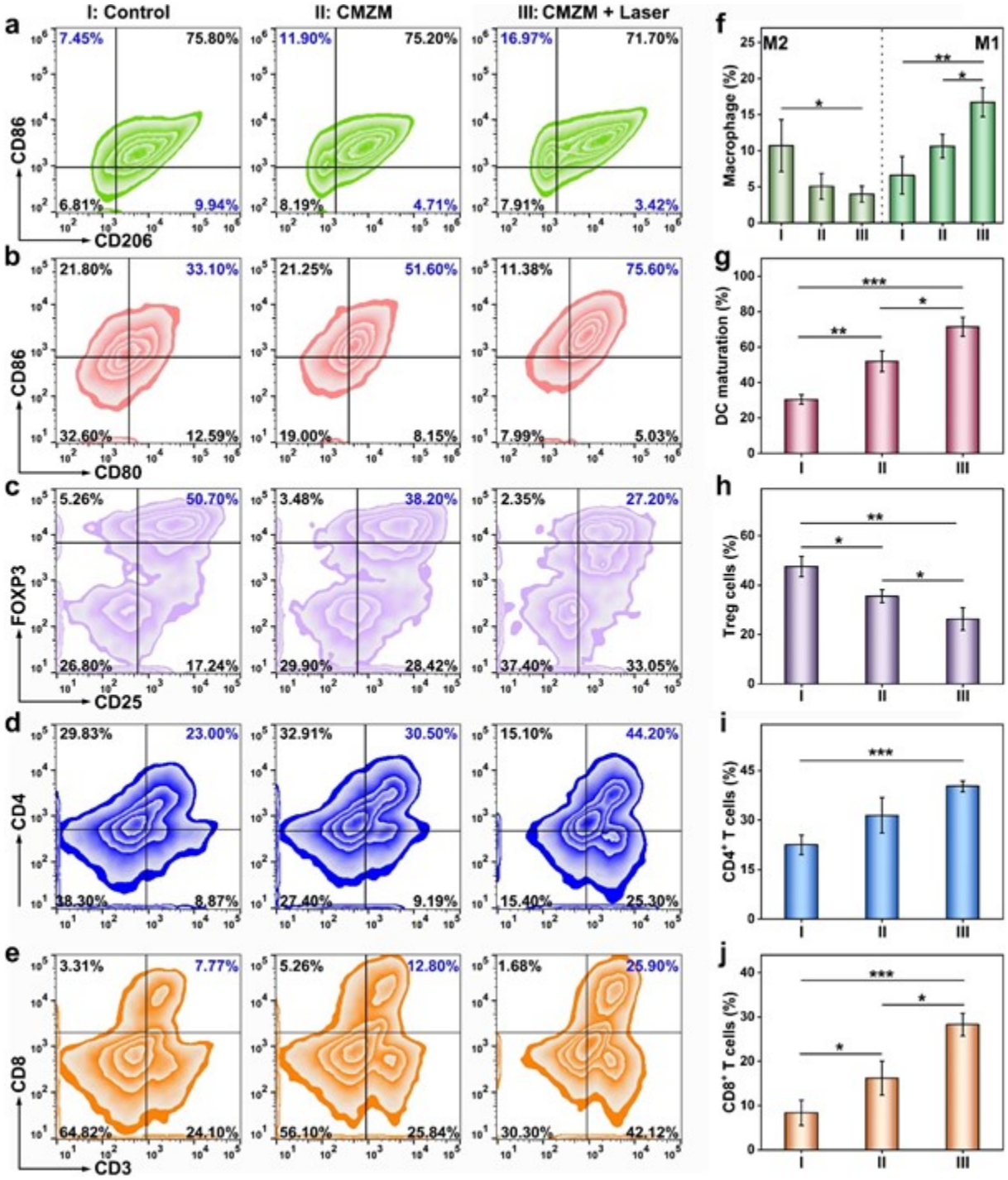

Figure 5. *In vivo* immune activated by CMZM. (a-e) Representative FCM plots and (f-j) the corresponding quantitative analysis on the proportion of tumor-infiltrating M2 phenotype and M1 phenotype TAMs,

mature dendritic cells, Treg cells, $CD4^+$ CTL, and $CD8^+$ CTL in the 4T1 tumor-bearing Balb/c mouse post *i.v.* injection of CMZM for 7 days (mean ± SD, $n = 3$, $^*p < 0.05$, $^{**}p < 0.01$, and $^{***}p < 0.001$).

2.5 *In Vivo* Immunotherapy Effect Evaluation

Ideal antitumor therapy must be able to eliminate the local tumor and inhibit tumor metastasis by activating systemic immune responses. Motivated by the high efficiency of CMZM in promoting ROS generation and activating the host immune response, bilateral 4T1 tumor-bearing mice were used to estimate the *in vivo* antitumor effect of ICB-based immunotherapy with anti-PD-L1 antibody (α-PD-L1). Subsequently, the mice were randomly divided into five groups (five per group) and subjected to various treatments (I: PBS, II: CMZM, III: CMZM + laser, IV: CMZM plus α-PD-L1, V: CMZM + laser plus α-PD-L1) at the 4^{th}, 6^{th}, 8^{th}, and 10^{th} day of distant tumor inoculation. The ICB inhibitor of α-PD-L1 was used to boost the immunotherapy effect in the plus α-PD-L1 groups (Figure 6a).

In the PBS group, primary and distant tumors grew rapidly, with an average volume increase from 104 to 947 mm^3 (8-fold increase) and 32 to 372 mm^3 (10.5-fold increase) after a 14-day treatment, respectively (Figure 6b,e). The primary and distant tumors in the CMZM group showed a certain degree of inhibition (3.9-fold and 4.3-fold increase, respectively) compared with that in the PBS group because of their superior tumor-targeting efficacy and multienzyme-mimicking features; however, the tumor suppression effects were unsatisfactory owing to the activation of weak immune responses. With the aid of PDT (0.1 W cm^{-2}, 5 min) in the CMZM plus laser groups, both the inhibition effect of primary and distant tumors were improved slightly. CDT and PDT with low-dose administration of CMZM were performed to cause the necrosis of partial tumor cells, which induces an immune response and reduce the toxicity and side effects of drugs. The outstanding potency of

tumor growth inhibition was achieved once CMZM was combined with α-PD-L1 immunotherapy. Both primary (Figure 6c,d) and distant (Figure 6f,g) tumors in the CDT&PDT&ICB synergy therapy group showed the lowest growth rate and minimal volumes and weights at the end of therapy. The body weights of all mice remained balanced during the therapy period, suggesting negligible systemic toxicity of CMZM (Figure S25). The tumor growth inhibition rates of the CMZM + α-PD-L1 and CMZM plus laser + α-PD-L1 groups were calculated to be 91.7% and 98.9% for primary tumors and 87.8% and 99.2% for distant tumors, respectively (Figure S26). In addition, tumor slices in the CMZM + α-PD-L1 and CMZM + laser plus α-PD-L1 groups displayed significant destruction, as observed by hematoxylin and eosin (H&E) staining, whereas other groups without α-PD-L1 administration exhibited mediocre or negligible lesions. An extraordinary therapeutic effect was verified by the TUNEL and Ki-67 staining of tumor sections (Figure S27). These results substantiated that the therapeutic efficiency of this synergistic therapy system with CDT, PDT, and ICB immunotherapy was better than that of the other groups, thereby suggesting an excellent synergistic effect of CMZM based on the preferable nanozyme activity and ICB strategy.

The severity of an immune reaction against a tumor is directly reflected by the number of cytotoxic T lymphocytes and helper T cells.[27] Considering that the immune response of distal tumors reflects the immune activation of primary tumors and the whole body,[28] infiltrating $CD4^+$ T cells (helper T cells) and $CD8^+$ T cells (CTLs) in distant tumors were determined using immunofluorescence staining. The immune cells were almost absent in the PBS group. However, the CMZM and CMZM + laser groups displayed moderate fluorescence of $CD4^+$ T cells and $CD8^+$ T cells infiltrating the tumors, which indicates a significant reversal of the immunosuppressive TME by ROS generation. The infiltrated $CD4^+$ and $CD8^+$ T cells in groups IV and V were further elevated after integration with ICB immunotherapy, which suggests that CMZM-mediated CDT and PDT created an

advantageous immunological microenvironment for immunotherapy (Figure 6h–j).

In addition to immune-related cells, cytokines play a key role in eliciting immune responses.[29] For example, TNF-α is an endogenous pyrogen that promotes tumor apoptosis and regulates the function of immune cells.[30] Interleukin-6 (IL-6), interleukin-12 (IL-12), and interleukin-16 (IL-16) play important roles in the inflammatory response and activate immune cells,[31] whereas IL-10 plays a negative role in immunoregulatory effects.[32] Based on the ELISA assay results, the positive immunoregulatory cytokine TNF-α, IL-6, IL-12, and IL-16 in the control group were 224.5 ng mL^{-1}, 49.7 pg mL^{-1}, 5.1 ng mL^{-1}, and 24.1 ng mL^{-1}, respectively. However, they increased by 2.0-, 2.1-, 4.5, and 1.6 folds in group V. Further, the level of the negative immunoregulatory cytokine IL-10 decreased gradually in groups I to V (Figure 6k and Figure S28). These outcomes indicate that robust immune responses *in vivo* are elicited by nanozyme-mediated CDT, PDT, and ICB therapies. The primary organs and blood of mice in all treatment groups were obtained for H&E staining and biochemical analyses to further evaluate the biocompatibility of CMZM. These results demonstrated no obvious inflammation or lesions in any organ, and the blood biochemical indices in all groups were within normal limits (Figure S29), thereby validating its negligible toxicity and safe application in the biomedical field.

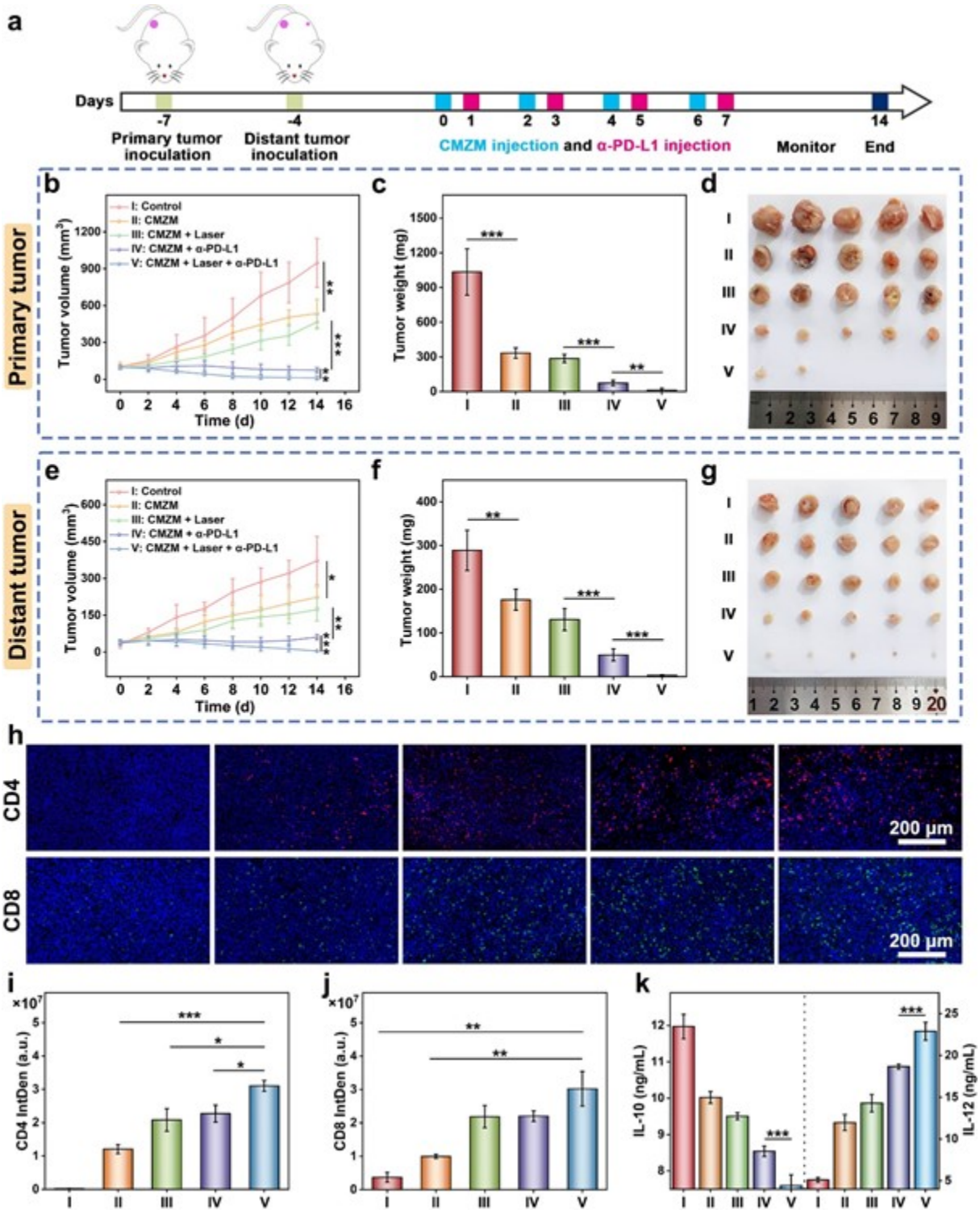

Figure 6. *In vivo* CMZM-mediated immunotherapy integrated with ICB strategy to resist primary and distant 4T1 tumors. (a) Schematic illustration of bilateral 4T1 tumor therapeutic schedule. (b,e) Time-

dependent primary and distant average tumor growth curves (mean ± SD, n = 5, *p < 0.05, **p < 0.01, and ***p < 0.001), (c,f) average tumor weights (mean ± SD, n = 5, **p < 0.01, and ***p < 0.001), and (d,g) resect tumors photo of bilateral 4T1 tumor-bearing mice after various treatments. (h-j) CD4 and CD8-stained tumor slices in various treatments and the corresponding fluorescence quantification analysis of $CD4^+$ and $CD8^+$ T cells in various groups (mean ± SD, n = 3, *p < 0.05, **p < 0.01, and ***p < 0.001). (k) The concentration of IL-10 and IL-12 in the serum of mice post various treatments (mean ± SD, n = 3, ***p < 0.001).

3. Conclusions

Excellent *in vitro* and *in vivo* tumor cell ablation was achieved via the synergistic effects of CDT, PDT, and ICB-based immunotherapy by utilizing the advantages of a well-designed CMZM. This study provides an ingenious strategy to promote cancer immunotherapy by reversing the immunosuppressive TME through the severe disruption of ROS homeostasis. Unlike most biomaterials with nanozyme activity, CMZM can increase the production of ROS through SOD-like, CAT-like, POD-like, and GSHOx-like activities. Furthermore, the CMZM collapsed under overexpressed GSH and acidic TME, enhancing $^{19}F/^{1}H$ T_1-weighted MRI and FLI of the tumor by the release of TFMIM, Mn ions, and Ce6. Remarkably, ^{19}F NMR allowed the determination of both the peroxidase (POD)-like and glutathione oxidase (GSHOx)-like activities of CMZM. This represents a novel protocol for monitoring the multifunctional enzyme-like activities of nanozymes and has the potential for several *in vivo* applications. The precise determination of tumor location is achievable through the utilization of the TME-activated $FL/^{1}H/^{19}F$ MR multimodal imaging technique. This approach bears the potential to facilitate real-time monitoring of tumor growth during immunotherapy. Immunosuppressive TME can be reversed by relieving tumor hypoxia and an acidic environment,

which facilitates the polarization of M2 macrophages to the M1 phenotype. Further, TAAs induced by sufficient ROS can accelerate DC maturation and the infiltration of CTLs into the tumor. Ultimately, the introduction of α-PD-L1 results in the complete inhibition of both primary and distant tumors. Consequently, this approach holds significant promise for potential future clinical applications.

4. Experimental Section

Fabrication of CMZM: Fluoride ZIF-8 doped with Mn (MZ) was synthesized in a manner similar to ZIF-8 by replacing Zn^{2+} with Mn^{2+} and partially replacing 2-MIM with TFMIM. $Zn(OAc)_2{\cdot}2H_2O$ (0.5 mM), manganese acetylacetonate (0.5 mM), 2-MIM (6.4 mM), TFMIM (1.6 mM), and $NH_3{\cdot}H_2O$ (300 µL) were mixed in a 50 mL methanol. The mixture was stirred at 25°C for 24 h and then centrifuged (10000 *g*, 10 min) to obtain MZ. Subsequently, Ce6 was loaded into the MZ; 5 mL of MZ (10 mg mL^{-1}) was mixed with 50 µL Ce6 (10 mg mL^{-1}). After stirring in the dark for 24 h (25°C), the mixture was centrifuged (10000 *g*, 10 min) to acquire Ce6@MZ (CMZ). The loading amounts of Ce6 in CMZ were determined using UV–vis–NIR absorption spectroscopy. Furthermore, the 4T1 cell membrane was collected and coated onto the CMZ. The 4T1 tumor cell membrane was extracted using a membrane protein extraction kit. Finally, the 4T1 cell membrane solution was mixed with an equal mass of the CMZ under stirring and suffered from the disruption via an ultrasonic probe at a power of 40% (2 s on, and 2 s off, 10 min), and the 4T1 cell membrane coated CMZ (CMZM) were acquired after centrifugation (4°C, 10000 *g*, 10 min).

In Vitro Macrophage Polarization: RAW264.7 macrophages (1×10^5) were seeded into 6-well plates and cultured for 12 h (37°C). IL-4 (30 ng mL^{-1}) was used to induce M2 polarization for 12 h. Then, RAW264.7 macrophages were cultured with residues of 4T1 cells after different treatments

(PBS, CMZM, and CMZM plus 660 nm laser) using the indirect coculture technique in a transwell chamber system. Finally, RAW264.7 macrophages were collected, stained with BV421 anti-F4/80, PE anti-CD86, and APC anti-CD206 antibodies, and measured by flow cytometry (Beckman Coulter).

In Vivo $^{1}H/^{19}F$ MRI: *In vivo* ^{1}H T_1-weighed MRI and ^{19}F MRI were performed using a 9.4 T micro-imaging system (Bruker Avance 400, Ettlingen, Germany). When the volume of the tumor reached approximately 100 mm^3, the 4T1 tumor-bearing mice were *i.v.* injected with CMZM (10 mg kg^{-1}) and ^{1}H T_1-weighed MRI was performed with a RARE sequence (TR = 500 ms, TE = 10 ms, FOV = 3.5 cm × 3.5 cm, 1 mm slice thickness, RARE factor = 2, matrix size = 256 × 256) at 0, 2, 4, 8, 12, 24, and 36 h. For *in vivo* ^{19}F MRI, the tumor was intratumorally injected with 50 µL of CMZM (C_{TFMIM} = 30 mM). After a ^{1}H MRI scan using a RARE sequence (TR = 500 ms, TE = 10 ms, FOV = 3.5 cm × 3.5 cm, 1 mm slice thickness, RARE factor = 2, matrix size = 256 × 256), ^{19}F MRI was conducted using a RARE sequence (TR = 500 ms, TE = 3 ms, FOV = 4.32 cm × 4.32 cm, 14.8 mm slice thickness, matrix size = 32 × 32, 64 averages).

In Vivo Antitumor Immunity Activation: When the subcutaneous 4T1 tumor reaches approximately 100 mm^3, BALB/c mice were randomly divided into three groups (n = 3): I) PBS, II) CMZM, and III) CMZM plus 660 nm laser (0.1 W cm^{-2}, 5 min). BALB/c mice were *i.v.* injected with PBS or CMZM (200 µL, 20 mg kg^{-1}). After seven days, the tumors were collected, minced, homogenized, and enzymatically digested to prepare single-cell suspensions for subsequent antibody labeling. Then, M2 macrophages ($CD86^-CD206^+F4/80^+$), M1 macrophages ($CD86^+CD206^-F4/80^+$), $CD4^+$ T cells ($CD3^+CD4^+CD8^-$), $CD8^+$ T cells ($CD3^+CD4^-CD8^+$), Tregs ($CD3^+CD25^+FOXP3^+$), and dendritic cells ($CD80^+CD86^+$) inside the tumor tissues were stained with corresponding commercial fluorophores instructions and analyzed by the flow cytometry (Beckman Coulter) instructions.

In Vivo Combined Immunotherapy in a Bilateral Tumor Model: The bilateral 4T1 tumor model was built by subcutaneously injecting 4T1 cells (5×10^6) suspended in 100 µL PBS into the right and left flanks of each mouse as the primary or distant tumors on day -7 and day -4, respectively. After four days, bilateral 4T1 tumor-bearing BALB/c mice were randomly allocated to five groups (n = 5) and treated as follows: (I) PBS, (II) CMZM, (III) CMZM + laser, (IV) CMZM + α-PD-L1, and (V) CMZM + laser plus α-PD-L1. Until the primary tumor volume reached 80 mm^3, PBS or CMZM (100 µL, 20 mg kg^{-1}) was *i.v.* injected into the mice on days 0, 2, 4, and 6. α-PD-L1 (25 µg per mouse) was *i.v.* injected into the mice of the corresponding groups on days 1, 3, 5, and 7. Tumor volumes were measured every two days, and the body weights were determined simultaneously. Tumor volume = length × $width^2/2$.

Another batch of bilateral 4T1 tumor models was used as previously described to further investigate the immune mechanism (n = 3). The mice were sacrificed two days after the last injection of anti-PD-L1, and distant tumors and the serum were collected. Tumor-infiltrating $CD4^+$ and $CD8^+$ T cells were analyzed by immunohistochemical staining. The serum with concentrations of TNF-α, IL-4, IL-6, IL-10, and IL-12 was analyzed by corresponding ELISA kits according to vendors' instructions.

Statistical Analysis: All the data are presented as mean ± SD. Experiments were performed in triplicate unless otherwise stated. A one-way analysis of variance was used to determine the significance of the difference. (*****$p < 0.05$, ******$p < 0.01$, *******$p < 0.001$).

Supporting Information

Supporting Information is available from the Wiley Online Library or the author.

Ackonwledgements

Ruifang Wang, Maosong Qiu, and Lei Zhang contributed equally to this work. This work was supported by the National Key R&D Program of China (2018YFA0704000), the National Natural Science Foundation of China (U21A20392, 82127802, 21921004, and 81901737), the Hubei Provincial Natural Science Foundation of China (grant no. 05182321). Xin Zhou acknowledges the support from the Tencent Foundation through the XPLORER PRIZE, and Shizhen Chen acknowledges the support from the Young Top-notch Talent Cultivation Program of Hubei Province.

Conflict of Interest

The authors declare no conflict of interest.

Data Availability Statement

The data that support the findings of this study are available from the corresponding author upon reasonable request.

Keywords

MRI, enzymatic cascade reactions, tumor cell membrane, α-PD-L1, immunotherapy.

Received: ((will be filled in by the editorial staff))
Revised: ((will be filled in by the editorial staff))
Published online: ((will be filled in by the editorial staff))

References

[1] R. S. Riley, C. H. June, R. Langer, M. J. Mitchell, *Nat. Rev. Drug. Discov.* **2019**, 18, 175.

[2] a) N. Budimir, G. D. Thomas, J. S. Dolina, S. Salek-Ardakani, *Cancer Immunol. Res.* **2022**, 10, 146; b) M. Nishino, N. H. Ramaiya, H. Hatabu, F. S. Hodi, *Nat. Rev. Clin. Oncol.* **2017**, 14, 655; c) B. Liu, Y. Zhang, D. Wang, X. Hu, Z. Zhang, *Nat. Cancer* **2022**, 3, 1123.

[3] a) D. Zeng, J. Wu, H. Luo, Y. Li, J. Xiao, J. Peng, Z. Ye, R. Zhou, Y. Yu, G. Wang, N. Huang, J. Wu, X. Rong, L. Sun, H. Sun, W. Qiu, Y. Xue, J. Bin, Y. Liao, N. Li, M. Shi, K. M. Kim, W. Liao, *J. Immunother. Cancer* **2021**, 9, e002467; b) X. D. Liu, W. Kong, C. B. Peterson, D. J. McGrail, A. Hoang, X. Zhang, T. Lam, P. G. Pilie, H. Zhu, K. E. Beckermann, S. M. Haake, S. Isgandrova, M. Martinez-Moczygemba, N. Sahni, N. M. Tannir, S. Y. Lin, W. K. Rathmell, E. Jonasch, *Nat. Commun.* **2020**, 11, 2135; c) D. M. Francis, M. P. Manspeaker, A. Schudel, L. F. Sestito, M. J. O'Melia, H. T. Kissick, B. P. Pollack, E. K. Waller, S. N. Thomas, *Sci. Transl. Med.* **2020**, 12, eaay3575.

[4] N. Erin, J. Grahovac, A. Brozovic, T. Efferth, *Drug. Resist. Updat.* **2020**, 53, 100715.

[5] a) T. Liu, C. Zhu, X. Chen, G. Guan, C. Zou, S. Shen, J. Wu, Y. Wang, Z. Lin, L. Chen, P. Cheng, W. Cheng, A. Wu, *Neuro. Oncol.* **2022**, 24, 1113; b) C. Liu, X. Liu, X. Xiang, X. Pang, S. Chen, Y. Zhang, E. Ren, L. Zhang, X. Liu, P. Lv, X. Wang, W. Luo, N. Xia, X. Chen, G. Liu, *Nat. Nanotechnol.* **2022**, 17, 531; c) H. Zhang, P. Yu, V. S. Tomar, X. Chen, M. J. Atherton, Z. Lu, H. G. Zhang, S. Li, A. Ortiz, J. Gui, N. A. Leu, F. Yan, A. Blanco, M. L. Meyer-Ficca, R. G. Meyer, D. P. Beiting, J. Li, S. Nunez-Cruz, R. S. O'Connor, L. R. Johnson, A. J. Minn, S. S. George, C. Koumenis, J. A. Diehl, M. C. Milone, H. Zheng, S. Y. Fuchs, *Nat. Cancer* **2022**, 3, 808.

[6] X. Li, Q. Zhou, A. Japir, D. Dutta, N. Lu, Z. Ge, *ACS Nano* **2022**, 16, 14982.

[7] Y. Xiao, T. Zhang, X. Ma, Q. C. Yang, L. L. Yang, S. C. Yang, M. Liang, Z. Xu, Z. J. Sun, *Adv. Sci.* **2021**, 8, e2101840.

[8] a) Z. Zhao, S. Dong, Y. Liu, J. Wang, L. Ba, C. Zhang, X. Cao, C. Wu, P. Yang, *ACS Nano* **2022**, 16, 20400; b) B. Xu, Y. Cui, W. Wang, S. Li, C. Lyu, S. Wang, W. Bao, H. Wang, M. Qin, Z. Liu, W. Wei, H. Liu, *Adv. Mater.* **2020**, 32, e2003563.

[9] N. Tao, H. Li, L. Deng, S. Zhao, J. Ouyang, M. Wen, W. Chen, K. Zeng, C. Wei, Y. N. Liu, *ACS Nano*

2022, 16, 485.

[10] Y. Sang, F. Cao, W. Li, L. Zhang, Y. You, Q. Deng, K. Dong, J. Ren, X. Qu, *J. Am. Chem. Soc.* **2020**, 142, 5177.

[11] Q. Zeng, B. Bie, Q. Guo, Y. Yuan, Q. Han, X. Han, M. Chen, X. Zhang, Y. Yang, M. Liu, P. Liu, H. Deng, X. Zhou, *Proc. Natl. Acad. Sci. U.S.A.* **2020**, 117, 17558.

[12] Y. Wan, J. Fang, Y. Wang, J. Sun, Y. Sun, X. Sun, M. Qi, W. Li, C. Li, Y. Zhou, L. Xu, B. Dong, L. Wang, *Adv. Healthc. Mater.* **2021**, 10, e2101515.

[13] N. Singh, M. A. Savanur, S. Srivastava, P. D'Silva, G. Mugesh, *Angew. Chem. Int. Ed.* **2017**, 56, 14267.

[14] a) C. Cao, H. Zou, N. Yang, H. Li, Y. Cai, X. Song, J. Shao, P. Chen, X. Mou, W. Wang, X. Dong, *Adv. Mater.* **2021**, 33, e2106996; b) M. Chang, Z. Hou, M. Wang, C. Yang, R. Wang, F. Li, D. Liu, T. Peng, C. Li, J. Lin, *Angew. Chem. Int. Ed.* **2021**, 60, 12971; c) L. Zhang, Q. G. Tan, S. J. Xiao, G. P. Yang, Q. Q. Zheng, C. Sun, X. L. Mao, J. Q. Fan, R. P. Liang, J. D. Qiu, *Small* **2023**, 19, e2207798; d) Y. Zou, B. Jin, H. Li, X. Wu, Y. Liu, H. Zhao, D. Zhong, L. Wang, W. Chen, M. Wen, Y. N. Liu, *ACS Nano* **2022**, 16, 21491.

[15] a) G. Guan, C. Zhang, H. Liu, Y. Wang, Z. Dong, C. Lu, B. Nan, R. Yue, X. Yin, X. B. Zhang, G. Song, *Angew. Chem. Int. Ed.* **2022**, 61, e202117229; b) Y. Yang, B. Wang, X. Zhang, H. Li, S. Yue, Y. Zhang, Y. Yang, M. Liu, C. Ye, P. Huang, X. Zhou, *Adv. Mater.* **2023**, 35, e2211337.

[16] S. Chen, L. Xiao, Y. Li, M. Qiu, Y. Yuan, R. Zhou, C. Li, L. Zhang, Z. X. Jiang, M. Liu, X. Zhou, *Angew. Chem. Int. Ed.* **2022**, 61, e202213495.

[17] a) Y. Li, H. Zhang, C. Guo, G. Hu, L. Wang, *Anal Chem* **2020**, 92, 11739; b) Y. Wang, Y. Li, Z. Zhang, L. Wang, D. Wang, B. Z. Tang, *Adv. Mater.* **2021**, 33, e2103748; c) T. Xiao, M. He, F. Xu, Y. Fan, B. Jia, M. Shen, H. Wang, X. Shi, *ACS Nano* **2021**, 15, 20377.

[18] C. Jiang, L. Zhang, X. Xu, M. Qi, J. Zhang, S. He, Q. Tian, S. Song, *Adv. Sci.* **2021**, 8, e2102500.

[19] a) J. Xiong, M. Wu, J. Chen, Y. Liu, Y. Chen, G. Fan, Y. Liu, J. Cheng, Z. Wang, S. Wang, Y. Liu, W. Zhang, *ACS Nano* **2021**, 15, 19756; b) L. Rao, L. L. Bu, B. Cai, J. H. Xu, A. Li, W. F. Zhang, Z. J. Sun, S. S. Guo, W. Liu, T. H. Wang, X. Z. Zhao, *Adv. Mater.* **2016**, 28, 3460.

[20] a) R. K. Jain, *Science* **2005**, 307, 58; b) D. W. Siemann, *Cancer. Treat. Rev.* **2011**, 37, 63.

[21] a) Y. Cheng, C. Wen, Y. Sun, H. Yu, X. Yin, *Adv. Funct. Mater.* **2021**, 31, 2104378; b) T. Jia, Z. Wang, Q. Sun, S. Dong, J. Xu, F. Zhang, L. Feng, F. He, D. Yang, P. Yang, J. Lin, *Small* **2020**, 16, e2001343; c) Y. Liu, J. Yang, B. Liu, W. Cao, J. Zhang, Y. Yang, L. Ma, J. M. de la Fuente, J. Song, J. Ni, C. Zhang, D. Cui, *Nanomicro Lett* **2020**, 12, 127.

[22] A. Fernández, M. Vendrell, *Chem. Soc. Rev.* **2016**, 45, 1182.

[23] a) V. Gambardella, J. Castillo, N. Tarazona, F. Gimeno-Valiente, C. Martínez-Ciarpaglini, M. Cabeza-Segura, S. Roselló, D. Roda, M. Huerta, A. Cervantes, T. Fleitas, *Cancer. Treat. Rev.* **2020**, 86, 102015; b) G. Theocharidis, B. E. Thomas, D. Sarkar, H. L. Mumme, W. J. R. Pilcher, B. Dwivedi, T. Sandoval-Schaefer, R. F. Sîrbulescu, A. Kafanas, I. Mezghani, P. Wang, A. Lobao, I. S. Vlachos, B. Dash, H. C. Hsia, V. Horsley, S. S. Bhasin, A. Veves, M. Bhasin, *Nat. Commun.* **2022**, 13, 181.

[24] a) M. Zhang, X. Jin, M. Gao, Y. Zhang, B. Z. Tang, *Adv. Mater.* **2022**, 34, e2205701; b) F. Pisaneschi, S. T. Gammon, V. Paolillo, S. A. Qureshy, D. Piwnica-Worms, *Nat. Biotechnol.* **2022**, 40, 965; c) R. R. Zheng, L. P. Zhao, N. Yang, Z. X. Chen, R. J. Kong, C. Y. Huang, X. N. Rao, X. Chen, H. Cheng, S. Y. Li, *Small* **2022**, e2205694.

[25] a) J. Liu, X. Zhang, Y. Cheng, X. Cao, *Cell. Mol. Immunol.* **2021**, 18, 2461; b) A. Harari, M. Graciotti, M. Bassani-Sternberg, L. E. Kandalaft, *Nat. Rev. Drug. Discov.* **2020**, 19, 635; c) H. Jeong, C. S. Lee, J. Lee, J. Lee, H. S. Hwang, M. Lee, K. Na, *Adv. Sci.* **2021**, 8, e2100118.

[26] a) F. Baharom, R. A. Ramirez-Valdez, K. K. S. Tobin, H. Yamane, C. A. Dutertre, A. Khalilnezhad, G. V. Reynoso, V. L. Coble, G. M. Lynn, M. P. Mulè, A. J. Martins, J. P. Finnigan, X. M. Zhang, J. A. Hamerman, N. Bhardwaj, J. S. Tsang, H. D. Hickman, F. Ginhoux, A. S. Ishizuka, R. A. Seder, *Nat. Immunol.* **2021**, 22, 41; b) A. E. Marciscano, N. Anandasabapathy, *Semin. Immunol.* **2021**, 52, 101481; c) R. Yabe, S. H. Chung, M. A. Murayama, S. Kubo, K. Shimizu, Y. Akahori, T. Maruhashi, A. Seno, T. Kaifu, S. Saijo, Y. Iwakura, *Nat. Commun.* **2021**, 12, 94.

[27] a) W. Ni, J. Wu, H. Fang, Y. Feng, Y. Hu, L. Lin, J. Chen, F. Chen, H. Tian, *Nano lett.* **2021**, 21, 7796; b) Z. Li, Z. Chu, J. Yang, H. Qian, J. Xu, B. Chen, T. Tian, H. Chen, Y. Xu, F. Wang, *ACS Nano* **2022**, 16, 15471.

[28] a) B. Ding, P. Zheng, F. Jiang, Y. Zhao, M. Wang, M. Chang, P. Ma, J. Lin, *Angew. Chem. Int. Ed.* **2020**, 59, 16381; b) H. Pan, M. Zheng, A. Ma, L. Liu, L. Cai, *Adv. Mater.* **2021**, 33, e2100241.

[29] a) D. J. Propper, F. R. Balkwill, *Nat. Rev. Clin. Oncol.* **2022**, 19, 237; b) Y. Song, M. Li, N. Song, X. Liu, G. Wu, H. Zhou, J. Long, L. Shi, Z. Yu, *J. Am. Chem. Soc.* **2022**, 144, 6907.

[30] F. Liu, X. Ding, X. Xu, F. Wang, X. Chu, J. H. Jiang, *Angew. Chem. Int. Ed.* **2022**, 61, e202203243.

[31] a) M. Mehanny, T. Kroniger, M. Koch, J. Hoppstädter, D. Becher, A. K. Kiemer, C. M. Lehr, G. Fuhrmann, *Adv. Healthc. Mater.* **2022**, 11, e2101151; b) M. W. Teng, E. P. Bowman, J. J. McElwee, M. J. Smyth, J. L. Casanova, A. M. Cooper, D. J. Cua, *Nat. Med.* **2015**, 21, 719; c) L. Forcina, C. Franceschi, A. Musarò, *Ageing Res. Rev.* **2022**, 80, 101697.

[32] M. Saraiva, A. O'Garra, *Nat. Rev. Immunol.* **2010**, 10, 170.

Short Summary

A smart nanozyme with multiple activities, including superoxide dismutase, catalase, peroxidase, and glutathione oxidase, was designed to reverse the immunosuppressive tumor microenvironment of "cold" tumors and activate host immunity through nanozyme-mediated cascade reactions. After synergy with α-PD-L1 blocking antibody, the outstanding efficacy of immunotherapy was acquired by the guide of tumor microenvironment-activated fluorescence imaging /^{1}H/^{19}F dual-nuclei magnetic resonance imaging.